MATERIALS CHEMISTRY
FRONTIERS

CCS 中国化学会 CHINESE CHEMICAL SOCIETY
ICCAS
ROYAL SOCIETY OF CHEMISTRY

RESEARCH ARTICLE

View Article Online
View Journal | View Issue

Cite this: *Mater. Chem. Front.*, 2022, **6**, 2184

Nanoconfining red phosphorus within MOF-derived hierarchically porous carbon networks for high performance potassium storage†

Jinqian Cheng,[a] Zibin Liang,[a] Yingxiao Wu,[a] Degao Wang,[a] Tianjie Qiu,[a] Yanqun Tang,[a] Jinming Shi,[a] Dingguo Xia[a] and Ruqiang Zou *[ab]

Red phosphorus is a kind of promising anode material for potassium-ion batteries owing to its ideal theoretical capacity. Unfortunately, its wide application in potassium storage is greatly limited by the poor electrical conductivity and severe volume expansion in the electrochemical reaction process of red phosphorus. Combining red phosphorus with a porous carbon substrate is a potential approach to enhance the potassium storage performance of red phosphorus, which can greatly promote the mass/charge transfer process and ease the volume change. Herein, hierarchically porous carbon networks were fabricated by two-step pyrolysis to confine red phosphorus (P@HPCN) with outstanding specific capacity, rate capability and cycling performance for potassium storage. The resultant anode material delivered reversible capacities of 461.8 mA h g^{-1} at 0.1 A g^{-1} after 100 cycles and 155.7 mA h g^{-1} at 1 A g^{-1} after 2000 cycles. Further experiments implied that the ideal electrochemical performance of P@HPCN could be associated with the synergism between red phosphorus and hierarchically porous carbon networks. Moreover, combining with theoretical calculations, we found that secondary calcination could effectively remove pyrrolic and pyridinic nitrogen from the porous carbon component, leading to a higher phosphorus loading.

Received 24th March 2022,
Accepted 5th July 2022

DOI: 10.1039/d2qm00261b

rsc.li/frontiers-materials

Introduction

The development of a sustainable and environmentally friendly energy storage system with high performance is vital to the progress of our society.[1,2] Lithium-ion batteries (LIBs) are one of the most effective and mature energy storage systems, which are widely used in electric vehicles and portable electronics.[3,4] Unfortunately, their further development is severely impeded by the high cost and limited content of lithium.[5] Potassium-ion batteries (PIBs) are potential substitutes for LIBs on account of their lower cost, higher abundance and appropriate redox potential close to that of lithium.[6–10] Over the past few years, alloy-based materials (including P, Si, Sb, Sn, *etc.*) have been investigated as promising anode materials for PIBs.[11–14] Among them, red phosphorus-based materials have attracted wide attention by virtue of their low cost, decent voltage and ideal theoretical capacity.[15–17] However, the cyclability of red phosphorus-based materials is extremely poor owing to their severe volume change in the charge–discharge process, which leads to cracking and pulverization.[18] What is more, the low electrical conductivity of red phosphorus greatly limits its utilization efficiency and rate capability.[19] All these disadvantages above greatly hinder the further development of red phosphorus-based anode materials for potassium storage.

It has been proved that graphite, which has witnessed tremendous success in LIBs, can also store potassium with a decent reversible capacity.[20,21] However, the larger ion radius of potassium leads to the sluggish kinetics and severe volume change in the electrochemical reaction process, which discourages the wide application of graphite anode materials for PIBs.[22] Over the past few years, great effort has been devoted to introducing hierarchical pore structures and defects into carbon materials, aiming at improving the capacity and cycling stability of PIBs.[23–25] However, these carbon materials still face lots of problems, such as the unapparent voltage platform, limited energy density and low initial Coulomb efficiency, which may lead to unstable work voltage and the loss of active material. Considering all the factors mentioned above, the combination of red phosphorus and porous carbon can well make up for their respective shortcomings to achieve better electrochemical storage capability. For red phosphorus, the

[a] *Beijing Key Lab of Theory and Technology for Advanced Battery Material, Department of Materials Science and Engineering, College of Engineering, Peking University, Beijing, China. E-mail: rzou@pku.edu.cn*
[b] *Institute of Clean Energy, Peking University, Beijing, China*

† Electronic supplementary information (ESI) available. See DOI: https://doi.org/10.1039/d2qm00261b

carbon substrates in the composite can greatly enhance the electrical conductivity and ease the volume expansion.[26] For carbon, the embedding of red phosphorus not only greatly enhanced its energy density and offered a stable voltage platform, but also effectively reduced its specific surface area resulting in improved initial Coulomb efficiency.

Herein, we combined red phosphorus and hierarchically porous carbon networks (P@HPCN) as the anode material for PIBs. Hierarchically porous carbon networks (HPCNs) were prepared by two-step pyrolysis of a metal–organic framework (MOF) precursor, and secondary calcination was performed to remove nitrogen from porous carbon. By confining red phosphorus particles into the pores of the HPCN, a reversible alloying reaction of red phosphorus and potassium is achieved as micropores and mesopores can greatly ease the volume expansion of red phosphorus in the electrochemical reaction process, and the hierarchically porous network structure can well promote the mass and electron transfer. Therefore, P@HPCN demonstrated an excellent reversible capacity of 461.8 mA h g^{-1} at 0.1 A g^{-1} after 100 cycles. In addition, an outstanding specific capacity of 155.7 mA h g^{-1} at 1 A g^{-1} after 2000 cycles was achieved, which indicated the ultralong cycling life of P@HPCN. Moreover, the influence of nitrogen on loading phosphorus was also investigated by theoretical calculations. Our work not only designed an excellent anode composite for potassium storage, but also provided practicable ideas for designing a red phosphorus-based anode material with outstanding performance for PIBs.

Experimental section

Synthesis of $Zn(C_2N_3H_2)_2$ (MET-6)

MET-6 was prepared using a modified method at room temperature.[27] Typically, 5.0 g of $ZnCl_2$ was added into the solution of ethanol (50 mL), ammonium hydroxide (20 mL), water (75 mL), and *N*,*N*-dimethylformamide (DMF, 50 mL). Then, we dropwise added 6.26 mL 1*H*-1,2,3-triazole to the mixture and the obtained mixture was fully stirred for 24 h. Afterwards, we got the white product through filtration. Finally, the product was washed with ethanol 4 times, and then dried at 80 °C for 8 h.

Synthesis of CN and HPCN

CN was prepared by pyrolysis of the MET-6 precursor at 1000 °C for 2 h under a flowing argon atmosphere. And the obtained samples were further heated at 1150 °C for 2 h under a flowing argon atmosphere to prepare HPCNs.

Synthesis of P@HPCN

50 mg of red phosphorus powder was thoroughly mixed and ground with 50 mg of HPCN and then the obtained mixture was encapsulated into a quartz tube under vacuum, and then heated at 600 °C for 8 h. Afterwards, the temperature was reduced to 260 °C with a ramping rate of 1 °C min^{-1} and kept for 24 h to convert white phosphorus to red phosphorus. The resulting black powder was then washed with carbon disulfide several times in an argon-filled glovebox to remove the residual white phosphorus, and then dried at 60 °C under vacuum for 10 h to obtain the final product P@HPCN. P@CN was also synthesized by using red phosphorus and CN as the substrate.

Electrochemical measurements

The active materials, carbon black (Super P) and binder carboxymethylcellulose (CMC) were mixed in a weight ratio of 7 : 2 : 1 to prepare electrodes. A mixed slurry formed by adding deionized water was coated on cleaned Cu foil and then dried at 80 °C under vacuum for 12 h. Electrodes were cut into circular disks and the active mass loading was in the range between 0.47 and 0.77 mg·cm^{-2}. For PIBs, glass fibre and potassium metal were used as the separator and counter electrode, respectively. The mixed solution (1.0 M) of potassium bis(fluorosulfonyl)imide (KFSI), ethylene carbonate (EC) and diethyl carbonate (DEC) was used as the electrolyte. Coin batteries were assembled in an argon-filled glovebox. The CV measurements were applied by using the CHI 760E electrochemical workstation, and the cycling performances of batteries were tested in a voltage window of 0.01 V to 2.8 V (*vs.* K/K^+) on a Land test system.

Theoretical calculations

All the theoretical calculations were implemented in the Vienna *ab initio* Simulation Package (VASP).[28] The ion–-electron interaction was described by using the projector-augmented-wave (PAW) potential,[29] and the electron–electron interaction was described by the generalized gradient approximation (GGA) with the function of Perdew–Burke–Ernzerhof (PBE).[30] The energy cutoff for all the calculations was set as 520 eV, and the reciprocal space was sampled using a $3 \times 3 \times 1$ Monkhorst–Pack *k*-point mesh.[31] For all models in our work, the optimizations were set to 1×10^{-5} eV and 0.02 eV $Å^{-1}$. Moreover, we set a 30 Å vacuum layer to eliminate the mutual interference between two repeated layers.

Results and discussion

The detailed preparation procedure for P@HPCN is illustrated in Fig. 1a, which consists of a two-step pyrolysis process followed by red phosphorus loading. First, the Zn-based metal–organic framework (MET-6) was used as the sacrificial precursor to obtain carbon networks (CNs) by pyrolysis. And a secondary pyrolysis step was carried out to obtain the HPCN. Later, red phosphorus was evaporated and then encapsulated into the pores of the HPCN at 600 °C. As shown in SEM images, the porous carbon network structure was well reserved after the evaporation–condensation process (Fig. 1c and d). In addition, no aggregated red phosphorus particle was found in TEM images (Fig. 1e and f), which indicated the good dispersion of red phosphorus in the HPCN. Furthermore, the energy-dispersive X-ray spectroscopy (EDS) elemental mapping images

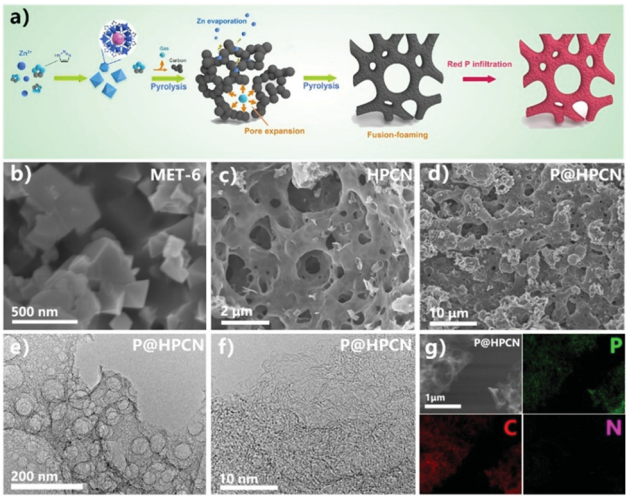

Fig. 1 (a) Schematic diagram of the preparation procedure for P@HPCN. (b) SEM image of MET-6. (c) SEM image of the HPCN. (d) SEM image, (e and f) TEM images, and (g) elemental mapping analysis of P@HPCN.

(Fig. 1g) also revealed the uniform distribution of red phosphorus in the HPCN.

As shown in the X-ray diffraction (XRD) patterns (Fig. 2a), P@CN displayed a peak at around 15.4°, which indicated the presence of red phosphorus.[32] For P@HPCN, this peak was not observed because of the high dispersion of red phosphorus in the HPCN. The Raman spectra showed two peaks located at 1354 and 1593 cm^{-1} (Fig. 2b), which corresponded to the D-band and G-band, respectively. And the I_G/I_D value increased after the secondary pyrolysis (Table S1, ESI†), which suggested an increased graphitization degree for the HPCN.[33] The pore structure of P@HPCN was investigated using nitrogen sorption measurements at 77 K (Fig. 2c), and it revealed that the HPCN had abundant mesoporous (4.0 nm) and micropores (1.2 and 1.5 nm). Compared with CNs (Fig. S8 and Table S2, ESI†), the types and amounts of pores significantly increased due to the removal of nitrogen. The results of elemental analysis (EA) measurement indicated that the nitrogen content of P@HPCN

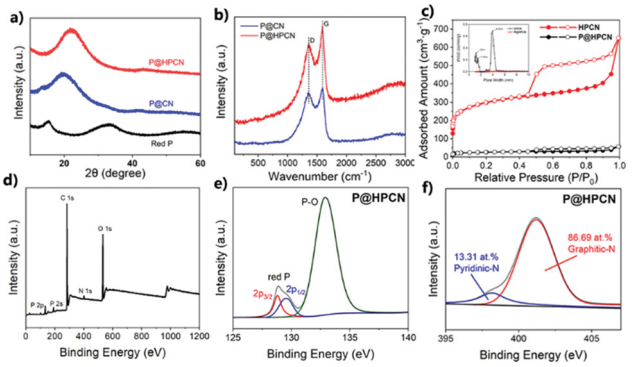

Fig. 2 (a) XRD patterns of P@HPCN, P@CN and red phosphorus. (b) Raman spectra of P@HPCN and P@CN. (c) Nitrogen adsorption and desorption isotherm with pore size distribution of HPCN and P@HPCN. (d) Full XPS spectrum, (e) P 2p spectrum, and (f) N 1s spectrum of P@HPCN.

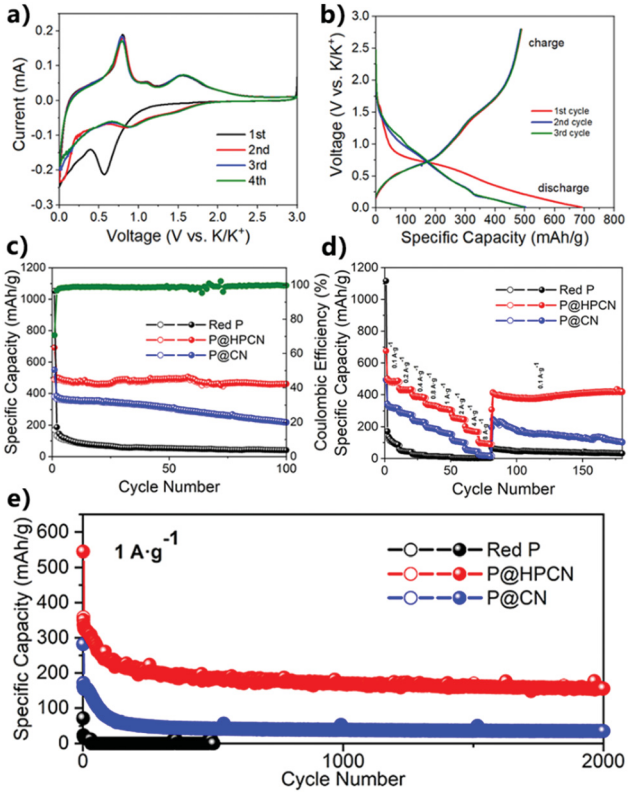

Fig. 3 (a) CV curves of P@HPCN at first several cycles. (b) GCD profiles of P@HPCN at 0.1 A g^{-1} at first several cycles. (c) Cycling performance of P@HPCN, P@CN and red phosphorus over 100 cycles at 0.1 A g^{-1}. (d) Rate performance of P@HPCN, P@CN and red phosphorus at various current densities. (e) Long-term cyclability of P@HPCN, P@CN and red phosphorus at 1 A g^{-1} over 2000 cycles.

(3.60 wt%) was less than that of P@CN (8.06 wt%), which confirmed the conjecture above. In addition, the nitrogen adsorbed amount of P@HPCN decreased rapidly, implying that red phosphorus was confined in the pores of the HPCN after the evaporation–condensation process. The elemental mass contents of P in P@CN and P@HPCN measured by inductive coupled plasma (ICP) were 22.3 wt% and 29.9 wt%, respectively, indicating that the nitrogen removal operation contributed to loading phosphorus. In some previous studies, it has been proved that the pyridinic and pyrrolic nitrogen components in porous carbon could promote the storage of potassium ions to some extent.[23,25] However, in our work, the removal of nitrogen might reduce the number of active nitrogen sites in porous carbon, but it also created a large amount of extra micropores and mesopores, which could well accommodate red phosphorus as new active sites with much higher potassium storage ability. The full X-ray photoelectron spectroscopy (XPS) spectrum indicated the presence of O, N, C and P in P@HPCN (Fig. 2d). In the high-resolution XPS spectrum of P 2p (Fig. 2e), two peaks centered at 128.87 eV and 129.54 eV were observed, which could be assigned to P $2p_{3/2}$ and P $2p_{1/2}$.[34] Furthermore, the peak with a binding energy of 132.92 eV could be attributed to the oxidation of red phosphorus in the measurement process.[35] In the high-resolution N 1s XPS spectrum (Fig. 2f),

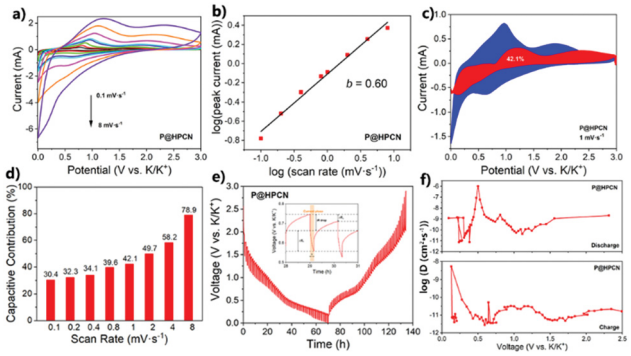

Fig. 4 (a) CV profiles of P@HPCN at various scan rates. (b) The corresponding *b* value plot. (c) The portion of capacitive contribution (red) in P@HPCN at a scan rate of 1 mV s^{-1}. (d) The plot of capacitive contribution in P@HPCN with respect to various scan rates. (e) The GITT profiles for P@HPCN in the discharge and charge processes. (f) The diffusion coefficients of potassium ions for P@HPCN.

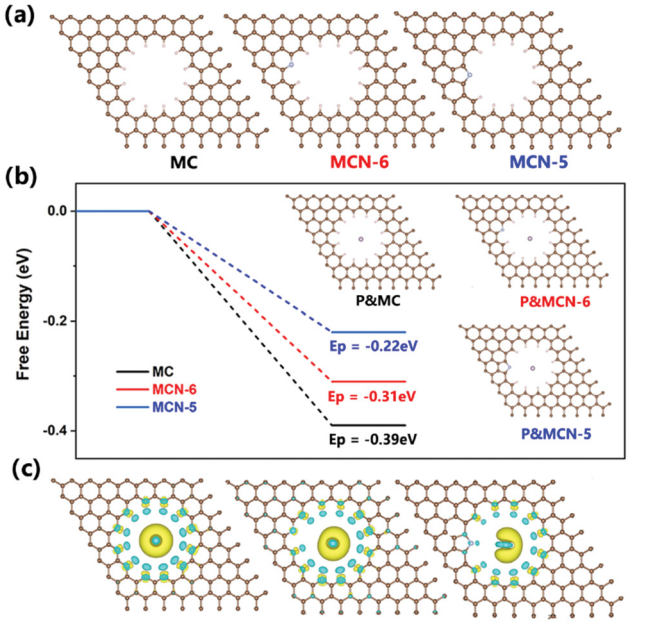

Fig. 5 (a) The structure plots of three types of carbon models. (b) Free energy diagrams for the introduction of phosphorus in different models. (c) The charge density difference profiles for different carbon models incorporated with phosphorus. Electron depletion and accumulation are displayed as blue and yellow areas, respectively.

two peaks located at 398.18 eV and 401.19 eV were observed, which could be attributed to pyridinic (13.31 at%) and graphitic nitrogen (86.69 at%).[36] Compared with P@CN (Fig. S9, ESI†), it can be seen that pyrrolic nitrogen was almost completely removed during the secondary pyrolysis process.

Fig. 3a shows the results of cyclic voltammetry (CV) measurements of P@HPCN, and a peak at about 0.57 V was observed in the first cycle, relating to the formation of the solid electrolyte interface (SEI) film.[37] During the following cycles, three pairs of redox peaks were observed, which were consistent with the voltage platforms in GCD profiles (Fig. 3b) and could be attributed to the stepwise alloying reactions between potassium and red phosphorus. Furthermore, there was a near-perfect overlap of CV curves after the first scan, implying the decent stability and reversibility of P@HPCN. The cycling stability of P@HPCN was also investigated in Fig. 3c. It could be seen that P@HPCN exhibited a high initial Coulombic efficiency of 70.7%. And P@HPCN also displayed a higher capacity of 461.8 mA h g^{-1} at 0.1 A g^{-1} after 100 cycles as compared with P@CN (219.8 mA h g^{-1}), which implied that the abundant pore structures of P@HPCN could efficiently confine phosphorus to achieve excellent electrochemical potassium storage performance. In addition, a distinct capacity decay was observed for pure red phosphorus, which suggested the positive effect of the porous carbon substrate. Fig. 3d displays the rate performance of P@HPCN, and we could see that P@HPCN delivered decent capacities of 433.2, 382.9, 328.6, 304.7, 244.8, 167.4, and 89.3 mA h g^{-1} at 0.2, 0.4, 0.8, 1, 2, 4 and 8 A g^{-1}, respectively, which are much higher than those of P@CN and pure red phosphorus, revealing the excellent rate capability of P@HPCN. Moreover, P@HPCN maintained excellent stability over the next 100 cycles as the current density returned to 0.1 A g^{-1}, delivering a capacity of 419.6 mA h g^{-1}. Long-term cyclability tests were carried out to further study the cycling stability of P@HPCN (Fig. 3e), and it displayed that P@HPCN had the highest capacity (155.7 mA h g^{-1}) at 1 A g^{-1} after 2000 cycles compared with P@CN and pure red phosphorus, indicating the remarkable cycling performance of P@HPCN.

To further investigate the kinetics of P@HPCN, the CV tests at various scan rates were performed (Fig. 4a). We calculated the *b* value using the equation: $i = a\nu^b$, where i and ν are the peak current and scan rate, and a and b are constants which can be adjusted. As is known, the value of b approaching 0.5 implies the diffusion-controlled process while the value of b approaching 1 reveals the capacitive process.[36] Fig. 4b shows the corresponding *b* value plot for P@HPCN, and the value of b is 0.60, implying that the potassium storage mechanism in P@HPCN is the diffusion-controlled process. The surface process contribution could be further quantitatively differentiated according to the equation:[38] $i = k_1\nu^{1/2} + k_2\nu$, where k_1 and k_2 represent the portions of the diffusion-controlled process (proportional to $\nu^{1/2}$) and the capacitive process (proportional to ν), respectively. The portion of capacitive contribution (red region) for P@HPCN at a scan rate of 1 mV s^{-1} is displayed in Fig. 4c, and was calculated to be 42.1%. Using similar analysis, we could know that the portion of capacitive contribution increased as the scan rate increased (Fig. 4d), which suggested that the capacitive process had a faster potassium storage kinetics compared with the diffusion-controlled process. Fig. 4e displays the results of galvanostatic intermittent titration (GITT) measurements, and the log(D_k)–V curve shows two obvious descending peaks corresponding to the stepwise alloying reactions between potassium and red phosphorus (Fig. 4f).

To further interpret our experimental results, we performed a theoretical calculation based on density functional theory (DFT) to evaluate the P-loading abilities of different carbon

structures. And three types of carbon models with different nitrogen doping were built (Fig. 5a), which were represented as MC, MCN-5 and MCN-6. It was calculated that the free energy changes of MCN-5, and MCN-6 for confining phosphorus were −0.22 and −0.31 eV, respectively (Fig. 5b), being higher than that of MC (−0.39 eV). Obvious charge redistribution between the carbon models and phosphorus was observed in charge density difference profiles (Fig. 5c), implying the interactions between them. Moreover, the charge density tended to accumulate less around the N-doping sites, indicating that the interaction between phosphorus and doped nitrogen was weaker.[25] Therefore, we found that the pyridinic and pyrrolic nitrogen components in porous carbon would impede the combination between the phosphorus and microporous carbon structure, which means that the removal of these nitrogen components can promote the loading of phosphorus, supporting the experimental results.

Conclusions

In conclusion, we presented a MOF-derived composite of red phosphorus and hierarchically porous carbon networks for potassium storage with outstanding specific capacity, rate capability and cyclability. By confining red phosphorus particles into pores, a reversible alloying reaction of red phosphorus and potassium is achieved as the porous carbon structure can greatly ease the volume expansion of red phosphorus in the charge–discharge process, and hierarchically porous carbon networks can well promote the electron and mass transport. In addition, the effect of nitrogen on loading phosphorus was demonstrated by theoretical calculations. Our work not only offered an excellent anode composite for potassium storage, but also provided practicable ideas for designing and fabricating red phosphorus-based anode materials with outstanding performance for PIBs.

Conflicts of interest

The authors declare that they have no conflict of interest.

Acknowledgements

This work was financially supported by the National Key Research and Development Program of China (2020YFA0210701), and the National Natural Science Foundation of China (52102199 and 51825201).

Notes and references

1 E. Pomerantseva, F. Bonaccorso, X. Feng, Y. Cui and Y. Gogotsi, Energy storage: The future enabled by nanomaterials, *Science*, 2019, **366**, eaan8285.
2 B. Dunn, H. Kamath and J. M. Tarascon, Electrical energy storage for the grid: a battery of choices, *Science*, 2011, **334**, 928–935.
3 D. Larcher and J. M. Tarascon, Towards greener and more sustainable batteries for electrical energy storage, *Nat. Chem.*, 2015, **7**, 19–29.
4 F. Wu, J. Maier and Y. Yu, Guidelines and trends for next-generation rechargeable lithium and lithium-ion batteries, *Chem. Soc. Rev.*, 2020, **49**, 1569–1614.
5 Q. Liu, S. Chen, X. Yu, L. Fan, J. Wang, T. Wang, R. Ma, X. Han and B. J. E. T. Lu, Low Cost and Superior Safety Industrial Grade Lithium Dual-Ion Batteries with a Second Life, *Energy Technol.*, 2018, **6**, 1994–2000.
6 W. Zhang, Y. Liu and Z. Guo, Approaching high-performance potassium-ion batteries *via* advanced design strategies and engineering, *Sci. Adv.*, 2019, **5**, eaav7412.
7 R. Rajagopalan, Y. G. Tang, X. B. Ji, C. K. Jia and H. Y. Wang, Advancements and Challenges in Potassium Ion Batteries: A Comprehensive Review, *Adv. Funct. Mater.*, 2020, **30**, 1909486.
8 D. Yang, C. Liu, X. Rui and Q. Yan, Embracing high performance potassium-ion batteries with phosphorus-based electrodes: a review, *Nanoscale*, 2019, **11**, 15402–15417.
9 C. Zhang, H. Zhao and Y. J. E. Lei, and E. Materials, Recent Research Progress of Anode Materials for Potassium-ion Batteries, *Energy Environ. Mater.*, 2020, **3**, 105–120.
10 Y. S. Xu, S. Y. Duan, Y. G. Sun, D. S. Bin, X. S. Tao, D. Zhang, Y. Liu, A. M. Cao and L. J. Wan, Recent developments in electrode materials for potassium-ion batteries, *J. Mater. Chem. A*, 2019, **7**, 4334–4352.
11 K. Song, C. Liu, L. Mi, S. Chou, W. Chen and C. J. S. Shen, Recent progress on the alloy-based anode for sodium-ion batteries and potassium-ion batteries, *Small*, 2021, **17**, 1903194.
12 W. Zhang, J. Mao, S. Li, Z. Chen and Z. Guo, Phosphorus-Based Alloy Materials for Advanced Potassium-Ion Battery Anode, *J. Am. Chem. Soc.*, 2017, **139**, 3316–3319.
13 S. H. Qi, J. W. Deng, W. C. Zhang, Y. Z. Feng and J. M. Ma, Recent advances in alloy-based anode materials for potassium ion batteries, *Rare Met.*, 2020, **39**, 970–988.
14 K. X. Lei, J. Wang, C. Chen, S. Y. Li, S. W. Wang, S. J. Zheng and F. J. Li, Recent progresses on alloy-based anodes for potassium-ion batteries, *Rare Met.*, 2020, **39**, 989–1004.
15 W. C. Chang, J. H. Wu, K. T. Chen and H. Y. J. A. S. Tuan, Red Phosphorus Potassium-Ion Battery Anodes, *Adv. Sci.*, 2019, **6**, 1801354.
16 Y. Wu, S. Hu, R. Xu, J. Wang, Z. Peng, Q. Zhang and Y. Yu, Boosting Potassium-Ion Battery Performance by Encapsulating Red Phosphorus in Free-Standing Nitrogen-Doped Porous Hollow Carbon Nanofibers, *Nano Lett.*, 2019, **19**, 1351–1358.
17 Z. Liang, T. Qiu, J. Cheng, Y. Tang, Y. Wu, J. Shi, S. Gao and R. J. B. Zou, and Supercaps, Nano-confining Red Phosphorus in a Carbon Hierarchical Superstructure for Superior Potassium Storage, *Batteries Supercaps*, 2021, **5**, e202100264.
18 P. Xiong, P. Bai, S. Tu, M. Cheng, J. Zhang, J. Sun and Y. J. S. Xu, Red Phosphorus Nanoparticle@ 3D Interconnected Carbon Nanosheet Framework Composite for Potassium-Ion Battery Anodes, *Small*, 2018, **14**, 1802140.

19 W. Li, S. Hu, X. Luo, Z. Li, X. Sun, M. Li, F. Liu and Y. J. A. M. Yu, Confined amorphous red phosphorus in MOF-derived N-doped microporous carbon as a superior anode for sodium-ion battery, *Adv. Mater.*, 2017, **29**, 1605820.
20 J. Zhao, X. X. Zou, Y. J. Zhu, Y. H. Xu and C. S. Wang, Electrochemical Intercalation of Potassium into Graphite, *Adv. Funct. Mater.*, 2016, **26**, 8103–8110.
21 W. Luo, J. Wan, B. Ozdemir, W. Bao, Y. Chen, J. Dai, H. Lin, Y. Xu, F. Gu, V. Barone and L. Hu, Potassium Ion Batteries with Graphitic Materials, *Nano Lett.*, 2015, **15**, 7671–7677.
22 D. Chao, W. Zhou, F. Xie, C. Ye, H. Li, M. Jaroniec and S. Z. Qiao, Roadmap for advanced aqueous batteries: From design of materials to applications, *Sci. Adv.*, 2020, **6**, eaba4098.
23 Z. Liang, Y. Wu, J. Cheng, Y. Tang, J. Shi, T. Qiu, W. Li, S. Gao, R. Zhong and R. J. S. Zou, A Metal–Organic Framework Nanorod-Assembled Superstructure and Its Derivative: Unraveling the Fast Potassium Storage Mechanism in Nitrogen-Modified Micropores, *Small*, 2021, **17**, 2100135.
24 H. N. He, D. Huang, Y. G. Tang, Q. Wang, X. B. Ji, H. Y. Wang and Z. P. Guo, Tuning nitrogen species in three-dimensional porous carbon via phosphorus doping for ultra-fast potassium storage, *Nano Energy*, 2019, **57**, 728–736.
25 Y. Xu, C. Zhang, M. Zhou, Q. Fu, C. Zhao, M. Wu and Y. Lei, Highly nitrogen doped carbon nanofibers with superior rate capability and cyclability for potassium ion batteries, *Nat. Commun.*, 2018, **9**, 1720.
26 X. Wu, W. Zhao, H. Wang, X. J. Qi, Z. Xing, Q. C. Zhuang and Z. C. Ju, Enhanced capacity of chemically bonded phosphorus/carbon composite as an anode material for potassium-ion batteries, *J. Power Sources*, 2018, **378**, 460–467.
27 R. Zhao, Z. Liang, S. Gao, C. Yang, B. Zhu, J. Zhao, C. Qu, R. Zou and Q. J. A. C. I. E. Xu, Puffing up energetic metal–organic frameworks to large carbon networks with hierarchical porosity and atomically dispersed metal sites, *Angew. Chem.*, 2019, **58**, 1975–1979.
28 G. Kresse and J. Furthmuller, Efficient iterative schemes for ab initio total-energy calculations using a plane-wave basis set, *Phys. Rev. B: Condens. Matter Mater. Phys.*, 1996, **54**, 11169–11186.
29 M. Gajdos, K. Hummer, G. Kresse, J. Furthmuller and F. Bechstedt, Linear optical properties in the projector-augmented wave methodology, *Phys. Rev. B: Condens. Matter Mater. Phys.*, 2006, **73**, 045112.
30 J. P. Perdew, K. Burke and M. Ernzerhof, Generalized gradient approximation made simple, *Phys. Rev. Lett.*, 1996, **77**, 3865–3868.
31 H. J. Monkhorst and J. D. Pack, Special Points for Brillouin-Zone Integrations, *Phys. Rev. B: Solid State*, 1976, **13**, 5188–5192.
32 Y. Wu, Z. Liu, X. Zhong, X. Cheng, Z. Fan and Y. Yu, Amorphous Red Phosphorus Embedded in Sandwiched Porous Carbon Enabling Superior Sodium Storage Performances, *Small*, 2018, **14**, e1703472.
33 C. Portet, G. Yushin and Y. Gogotsi, Electrochemical performance of carbon onions, nanodiamonds, carbon black and multiwalled nanotubes in electrical double layer capacitors, *Carbon*, 2007, **45**, 2511–2518.
34 F. Yang, H. Gao, J. Hao, S. Zhang, P. Li, Y. Liu, J. Chen and Z. J. A. F. M. Guo, Yolk–shell structured FeP@C nanoboxes as advanced anode materials for rechargeable lithium-/potassium-ion batteries, *Adv. Funct. Mater.*, 2019, **29**, 1808291.
35 X. J. Wang, K. Chen, G. Wang, X. J. Liu and H. Wang, Rational Design of Three-Dimensional Graphene Encapsulated with Hollow FeP@Carbon Nanocomposite as Outstanding Anode Material for Lithium Ion and Sodium Ion Batteries, *ACS Nano*, 2017, **11**, 11602–11616.
36 Z. Liang, Y. Wu, J. Cheng, Y. Tang, J. Shi, T. Qiu, W. Li, S. Gao, R. Zhong and R. J. S. Zou, A Metal–Organic Framework Nanorod-Assembled Superstructure and Its Derivative: Unraveling the Fast Potassium Storage Mechanism in Nitrogen-Modified Micropores, *Small*, 2021, **17**, 2100135.
37 I. Sultana, M. M. Rahman, S. Mateti, V. G. Ahmadabadi, A. M. Glushenkov and Y. J. N. Chen, K-ion and Na-ion storage performances of Co_3O_4–Fe_2O_3 nanoparticle-decorated super P carbon black prepared by a ball milling process, *Nanoscale*, 2017, **9**, 3646–3654.
38 T. Brezesinski, J. Wang, S. H. Tolbert and B. J. N. M. Dunn, Ordered mesoporous α-MoO_3 with iso-oriented nanocrystalline walls for thin-film pseudocapacitors, *Nat. Mater.*, 2010, **9**, 146–151.